RESEARCH ARTICLE

SusMat WILEY

Air-stable $Li_{3.12}P_{0.94}Bi_{0.06}S_{3.91}I_{0.18}$ solid-state electrolyte with high ionic conductivity and lithium anode compatibility toward high-performance all-solid-state lithium metal batteries

Daokuan Jin[1,2] | **Haodong Shi**[2] | **Yuxin Ma**[2,3] | **Yangyang Liu**[2] | **Yang Wang**[1,4] | **Yanfeng Dong**[5] | **Mingbo Wu**[1,4] | **Zhong-Shuai Wu**[2,6]

[1]State Key Laboratory of Heavy Oil Processing, Institute of New Energy, College of Chemistry and Chemical Engineering, China University of Petroleum (East China), Qingdao, China

[2]State Key Laboratory of Catalysis, Dalian Institute of Chemical Physics, Chinese Academy of Sciences, Dalian, China

[3]University of Chinese Academy of Sciences, Beijing, China

[4]College of New Energy, China University of Petroleum (East China), Qingdao, China

[5]Department of Chemistry, College of Sciences, Northeastern University, Shenyang, China

[6]Dalian National Laboratory for Clean Energy, Chinese Academy of Sciences, Dalian, China

Correspondence

Haodong Shi and Zhong-Shuai Wu, State Key Laboratory of Catalysis, Dalian Institute of Chemical Physics, Chinese Academy of Sciences, 457 Zhongshan Road, Dalian 116023, China.
Email: hdshi@dicp.ac.cn, wuzs@dicp.ac.cn

Mingbo Wu, State Key Laboratory of Heavy Oil Processing, Institute of New Energy, College of Chemistry and Chemical Engineering, China University of Petroleum (East China), Qingdao 266580, China.
Email: wumb@upc.edu.cn

Abstract

Sulfide solid-state electrolytes (SSEs) with superior ionic conductivity and processability are highly promising candidates for constructing all-solid-state lithium metal batteries (ASSLMBs). However, their practical applications are limited by their intrinsic air instability and serious interfacial incompatibility. Herein, a novel glass-ceramic electrolyte $Li_{3.12}P_{0.94}Bi_{0.06}S_{3.91}I_{0.18}$ was synthesized by co-doping Li_3PS_4 with Bi and I for high-performance ASSLMBs. Owing to the strong Bi–S bonds that are thermodynamically stable to water, increased unit cell volume and Li^+ concentration caused by P^{5+} substitution with Bi^{3+}, and the in situ formed robust solid electrolyte interphase layer LiI at lithium surface, the as-prepared $Li_{3.12}P_{0.94}Bi_{0.06}S_{3.91}I_{0.18}$ SSE achieved excellent air stability with a H_2S concentration of only 0.205 cm^3 g^{-1} (after 300 min of air exposure), outperforming Li_3PS_4 (0.632 cm^3 g^{-1}) and the most reported sulfide SSEs, together with high ionic conductivity of 4.05 mS cm^{-1}. Furthermore, the $Li_{3.12}P_{0.94}Bi_{0.06}S_{3.91}I_{0.18}$ effectively improved lithium metal stability. With this SSE, an ultralong cyclability of 700 h at 0.1 mA cm^{-2} was realized in a lithium symmetrical cell. Moreover, the $Li_{3.12}P_{0.94}Bi_{0.06}S_{3.91}I_{0.18}$-based ASSLMBs with $LiNi_{0.8}Mn_{0.1}Co_{0.1}O_2$ cathode achieved ultrastable capacity retention rate of 95.8% after 300 cycles at 0.1 C.

This work provides reliable strategy for designing advanced sulfide SSEs for commercial applications in ASSLMBs.

KEYWORDS

air stability, all-solid-state lithium metal battery, glass-ceramic, lithium metal compatibility, sulfide solid-state electrolyte

1 | INTRODUCTION

All-solid-state lithium metal batteries (ASSLMBs) represent a promising next-generation battery technology owing to their high energy density and superior safety characteristics in comparison to conventional lithium-ion batteries utilizing organic electrolytes.[1] As a vital component of ASSLMBs, solid-state electrolytes (SSEs), including oxide, sulfide, and polymer SSEs, have attracted extensive attention and made remarkable breakthroughs over the past decades.[2–5] Among them, sulfide-based glass-ceramic SSEs such as Li_3PS_4 have shown great promise for large-scale commercial application due to their straightforward preparation process and excellent ductility, facilitating tight solid–solid contact through simple cold pressing.[6–11] However, there are several key issues that are obstructing their development and practical application of sulfide SSEs in ASSLMBs, and the noteworthy one is their low ionic conductivity due to the disordered lattice structures, which limit the overall electrochemical performance of the battery. Additionally, severe side reactions occur between sulfide SSEs and lithium metal anodes, resulting in interfacial incompatibility, lithium dendrite formation, and eventual short-circuiting battery.[12–14] Moreover, due to the hydrolyzation and generation of H_2S toward moisture, the poor air stability of sulfide SSEs usually results in the structure/property degradation and increased fabrication costs.[3,15–20]

Currently, several effective strategies have been developed to conquer these challenges in glass-ceramic sulfide SSEs. Heterovalent element substitution is a typical and effective method to improve the ionic conductivity of SSEs.[21–25] For instance, Rajagopal et al. partially replaced the P^{5+} with larger atomic radius and higher polarization of Sb^{5+}, resulting in an improvement in ionic conductivity of $Li_7P_3S_{11}$ from 1.40 to 2.55 mS cm^{-1}.[26] Meanwhile, hard and soft acids and bases theory has been employed by the strategies of partially or completely replacing the hard acid P^{5+} with soft acid ions, and replacing S^{2-} with hard base ions to improve the air stability of SSEs.[23–25] Liu et al. used hard acid Zn^{2+} and hard base ions O^{2-} to partially replace P^{5+} and S^{2-}, respectively, which in turn enhanced air stability (exposure time 180 min, H_2S release 0.018 cm^3 g^{-1}) of Li_3PS_4.[27] Besides, the interface issues between SSEs and lithium metal anodes have been studied to realize their compatibility. In particular, the halide-rich sulfide SSEs can effectively suppress the side reactions and inhibit the growth of lithium dendrites through the in situ formation of a stable solid electrolyte interface (SEI) layer during battery operation.[1,22] For instance, $Li_{5.7}PS_{4.7}Cl_{1.3}$ achieved ASSLMBs with high reversible capacities and stable cyclability due to the formation of a LiCl-rich interface.[13] Despite great progress, it remains a significant challenge to develop an advanced sulfide SSE with superior ionic conductivity, high air stability, and lithium anode compatibility for achieving ASSLMBs with exceptional performance.[28–32]

In this work, we report the synthesis of novel glass-ceramic $Li_{3+2x}P_{1-x}Bi_xS_{4-1.5x}I_{3x}$ (x = 0, 0.02, 0.04, 0.06, 0.08) SSEs by co-doping Li_3PS_4 with BiI_3 for

high-performance ASSLMBs. Benefiting from the strong affinity of Bi^{3+} toward S^{2-}, enlarged lattice volume, high Li^+ ion concentration, and in situ formed artificial LiI SEI layer between the lithium metal anode and the SSE, the resulting $Li_{3.12}P_{0.94}Bi_{0.06}S_{3.91}I_{0.18}$ possesses excellent air stability, high ionic conductivity (4.05 mS cm^{-1}), as well as enhanced lithium metal interface compatibility. As a result, the symmetric lithium metal cells using $Li_{3.12}P_{0.94}Bi_{0.06}S_{3.91}I_{0.18}$ achieved superior dendrite suppression capability up to a high critical current density (CCD) of 0.9 mA cm^{-2} and ultralong cyclability of 700 h at 0.1 mA cm^{-2}. Moreover, the as-assembled ASSLMBs presented outstanding cycling stability (95.8% capacity retention after 300 cycles) and rate capability (169 mAh g^{-1} at 0.05 C, 87 mAh g^{-1} at 0.5 C), showcasing their promising applications for the next-generation high-energy-density ASSLMBs.

2 | RESULTS AND DISCUSSION

As shown in Figures 1A and S1, a series of $Li_{3+2x}P_{1-x}Bi_xS_{4-1.5x}I_{3x}$ (x = 0, 0.02, 0.04, 0.06, 0.08) SSEs were synthesized by ball milling and annealing of Li_2S, P_2S_5, and BiI_3. X-ray diffraction (XRD) measurements were performed to determine the effect of Bi and I co-doping amount on the structure of the SSEs (Figure 1B). The intensity of the crystalline peak of Li_3PS_4 at 31.1° gradually weakens until it disappears from x = 0.04. In contrast, the peak at 32.05° for $LiBiS_2$ appears, while the characteristic peak of BiI_3 is not found in the XRD patterns. The overall structure remains relatively unchanged, suggesting successful co-doping of Bi and I into the Li_3PS_4. Moreover, the Raman spectra provide further insights into the effect of Bi and I co-doping on the Li_3PS_4. As shown in Figure 1C, a characteristic peak at 418 cm^{-1} corresponds to the PS_4^{3-} tetrahedra, while no peak splitting or new group formation is observed, indicating that the Bi and I co-doping solely influences the P–S bond without altering the overall structure of PS_4^{3-}. Thus, the model of $Li_{3.12}P_{0.94}Bi_{0.06}S_{3.91}I_{0.18}$ can be constructed (Figure S2).

Taking $Li_{3.12}P_{0.94}Bi_{0.06}S_{3.91}I_{0.18}$ as a representative, the chemical bonding information was verified by X-ray photoelectron spectroscopy (XPS). The S 2p spectrum of Li_3PS_4 can be fitted into two distinct peaks, corresponding to P–S–Li (160.5 and 161.8 eV) and P = S bonds (161.1 and 162.4 eV), respectively (Figure 1D).[14] The P 2p spectrum peaks of Li_3PS_4 appear at 131.4 and 132.4 eV owing to the typical PS_4^{3-} (Figure 1E). In the case of $Li_{3.12}P_{0.94}Bi_{0.06}S_{3.91}I_{0.18}$, except the peaks corresponding to P = S and P–S–Li (161 and 162.7 eV), an additional peak primarily arises from the Bi 4f peak, and Bi–S peak is

observed.[14] Additionally, the increased peak intensity at 162.2 eV is attributed to the overlap of P–S and Bi–S peaks, resulting from Bi doping. No discernible difference in this peak between the two SEEs is observed in the Li 1s spectrum (Figure S3). However, one of the sulfur atoms in the PS_4^{3-} unit, originally presenting in Li_3PS_4, undergoes the substitution with one I atom. This substitution, denoted as PI_x (132.8 eV), is clearly visible in Figure 1E. Moreover, the I 3d spectrum exhibits two peaks at 618 and 630 eV (Figure S4), further confirming the doping of I into Li_3PS_4. The morphology of SSEs is presented in Figures 1F and S5, and both the Li_3PS_4 and $Li_{3.12}P_{0.94}Bi_{0.06}S_{3.91}I_{0.18}$ electrolyte particles exhibit irregular shapes with sizes ranging from 10 to 20 μm. The energy dispersive spectroscopy elemental profile of $Li_{3.12}P_{0.94}Bi_{0.06}S_{3.91}I_{0.18}$ confirmed the uniformly distributed P, S, Bi, and I in the electrolyte particles (Figure 1G), indicating the co-doping of both Bi and I into Li_3PS_4.

Electrochemical impedance spectroscopy (EIS) was conducted to evaluate the ionic conductivity of the as-prepared $Li_{3+2x}P_{1-x}Bi_xS_{4-1.5x}I_{3x}$ (x = 0, 0.02, 0.04, 0.06, 0.08) SSEs. It is evident that $Li_{3.12}P_{0.94}Bi_{0.06}S_{3.91}I_{0.18}$ (x = 0.06) shows the optimal ionic conductivity of 4.05 mS cm^{-1}, which is one order of magnitude higher than that of Li_3PS_4 (0.24 mS cm^{-1}, Figure 2A). Furthermore, the calculated activation energy (E_a) of $Li_{3.12}P_{0.94}Bi_{0.06}S_{3.91}I_{0.18}$ is as low as 0.252 eV (Figure 2B,C).[33] The high ionic conductivity with low activation barrier of $Li_{3.12}P_{0.94}Bi_{0.06}S_{3.91}I_{0.18}$ can be attributed to the synergy of increased Li^+ concentration, weakened charge interaction between part of Li^+ and S^{2-}, and anion site disorder induced by the insertion of I^-.[14,26] However, high amount of BiI_3 (x = 0.08) tends to induce the formation of impurity phases such as LiI, resulting in the obstructed Li^+ migration and a significant increase in the activation energy (E_a = 0.269 eV). In addition, from the direct current polarization curves, the $Li_{3.12}P_{0.94}Bi_{0.06}S_{3.91}I_{0.18}$ electrolyte exhibits the lower electronic conductivity of 1.0×10^{-8} S cm^{-1} compared with Li_3PS_4 (6.6×10^{-8} S cm^{-1}) (Figure 2D), which facilitates to prevent dendrite formation on the Li metal anode.[14] Moreover, differential thermal analysis of $Li_{3.12}P_{0.94}Bi_{0.06}S_{3.91}I_{0.18}$ was conducted with a heating rate of 10°C/min in an argon environment (Figure 2E), in which the crystallization temperature of $Li_{3.12}P_{0.94}Bi_{0.06}S_{3.91}I_{0.18}$ is determined to be 228°C. A highly crystalline SSEs can be obtained after annealing at 230°C for 4 h ($Li_{3.12}P_{0.94}Bi_{0.06}S_{3.91}I_{0.18}$-230) (Figure S6). However, the EIS plot of $Li_{3.12}P_{0.94}Bi_{0.06}S_{3.91}I_{0.18}$-230 shows a high impedance of 174 Ω and a low ionic conductivity of only 0.51 mS cm^{-1} compared to the glass-ceramic SSEs annealed at 210°C ($Li_{3.12}P_{0.94}Bi_{0.06}S_{3.91}I_{0.18}$-210) (4.05 mS cm^{-1}, Figure S7). The enhanced ionic conductivity of glass-ceramic phase is likely due to the self-organization
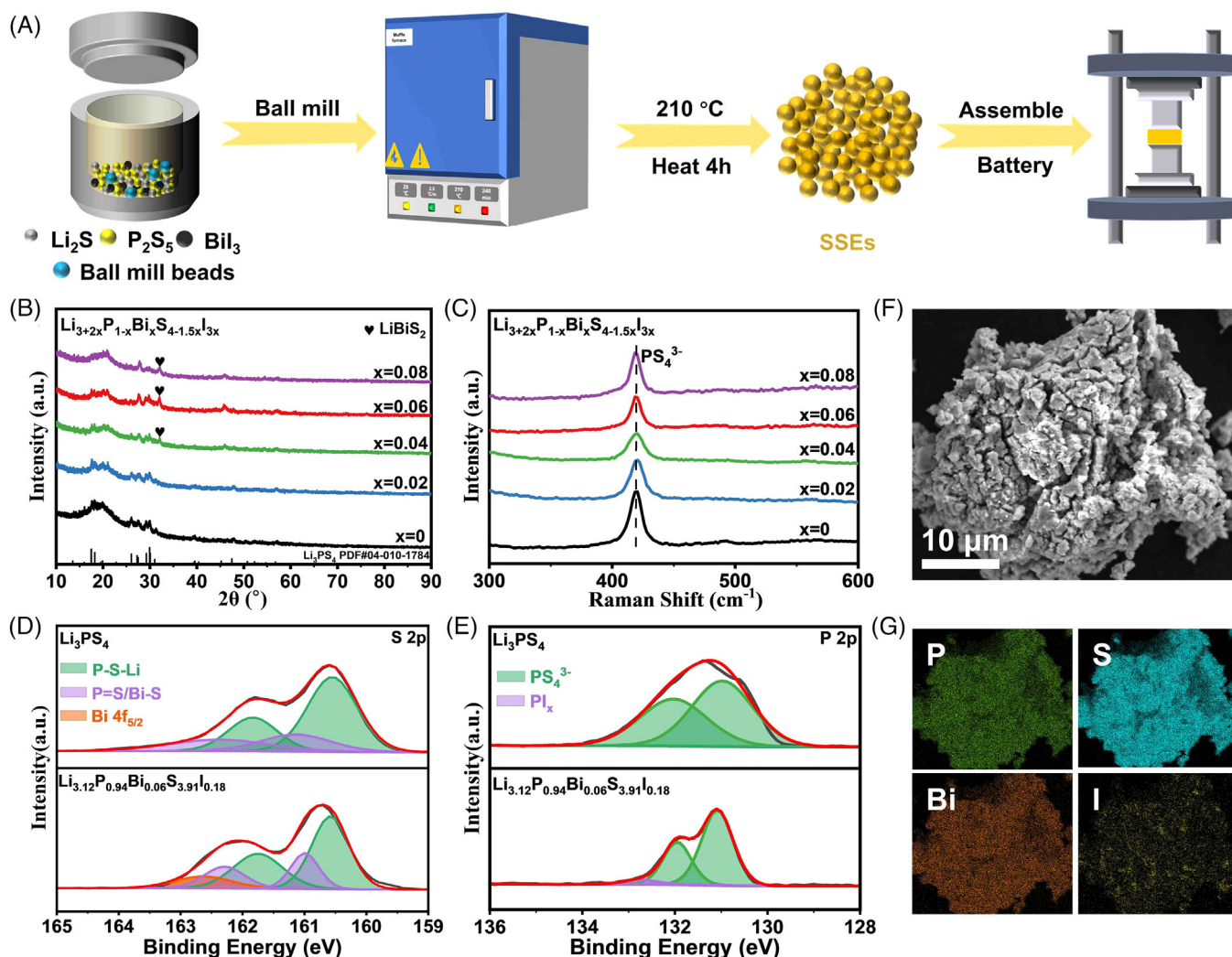
FIGURE 1 Preparation and crystal structure characterization of $Li_{3+2x}P_{1-x}Bi_xS_{4-1.5x}I_{3x}$ ($x = 0$, 0.02, 0.04, 0.06, and 0.08) SSEs. (A) Schematic diagram for the preparation of SSEs for all-solid-state lithium metal batteries (ASSLMBs). (B) X-ray diffraction (XRD) patterns and (C) Raman spectra of Li_3PS_4 and $Li_{3+2x}P_{1-x}Bi_xS_{4-1.5x}I_{3x}$ ($x = 0.02$, 0.04, 0.06, and 0.08). X-ray photoelectron spectroscopy (XPS) spectra of (D) S 2p and (E) P 2p for $Li_{3.12}P_{0.94}Bi_{0.06}S_{3.91}I_{0.18}$. (F) Scanning electron microscopy (SEM) image and (G) corresponding energy dispersive spectroscopy (EDS) elemental mapping of P, S, Bi, and I for $Li_{3.12}P_{0.94}Bi_{0.06}S_{3.91}I_{0.18}$.

of microcrystalline glasses into heterogeneous nanostructured domains during the solid-phase reaction.[34] It is worth noting that the low annealing temperature of 210°C achieving impressive ionic conductivity, which is obviously lower than the processing temperatures of common SSEs.[3,5,10] Thus, the synthesis cost can be significantly reduced, endowing $Li_{3+2x}P_{1-x}Bi_xS_{4-1.5x}I_{3x}$-210 a promising choice for ASSLMBs (Figure 2F).[35]

To evaluate the lithium dendrite suppression ability of the SSEs, the $Li|Li_{3+2x}P_{1-x}Bi_xS_{4-1.5x}I_{3x}|Li$ symmetric cells were assembled. Figure S8 shows the voltage curves of lithium plating and stripping, and the initial current density is 0.1 mA cm^{-2}, with the gradual increase in the current density. From the comparison, a sudden voltage drop occurs for $Li|Li_3PS_4|Li$ symmetric cell (Figure S8a), indicating a CCD value of 0.25 mA

cm^{-2} for Li_3PS_4. In a sharp contrast, the CCD value of $Li|Li_{3.12}P_{0.94}Bi_{0.06}S_{3.91}I_{0.18}|Li$ symmetric cells reaches a maximum value of 0.9 mA cm^{-2} (Figure S8d), obviously higher than those of $Li|Li_{3.04}P_{0.98}Bi_{0.02}S_{3.97}I_{0.06}|Li$ (0.25 mA cm^{-2}), $Li|Li_{3.08}P_{0.96}Bi_{0.04}S_{3.94}I_{0.12}|Li$ (0.20 mA cm^{-2}), and $Li|Li_{3.16}P_{0.92}Bi_{0.08}S_{3.88}I_{0.24}|Li$ (0.40 mA cm^{-2}) (Figure S8b–e), which is attributed to its intrinsic low electronic conductivity and high interface stability between Li metal and SSEs.[36] The long-term cyclability was also examined by Li metal symmetric cells at a current density of 0.1 mA cm^{-2} and a capacity of 0.1 mAh cm^{-2} (Figures 3A and S8f). The $Li|Li_{3.12}P_{0.94}Bi_{0.06}S_{3.91}I_{0.18}|Li$ symmetric cell maintains an ultra-stable overpotential of 13 mV without short circuiting for 700 h (Figures 3A–D and S9c,d). However, the $Li|Li_3PS_4|Li$ cell experiences a significant detectable overpotential alteration only after
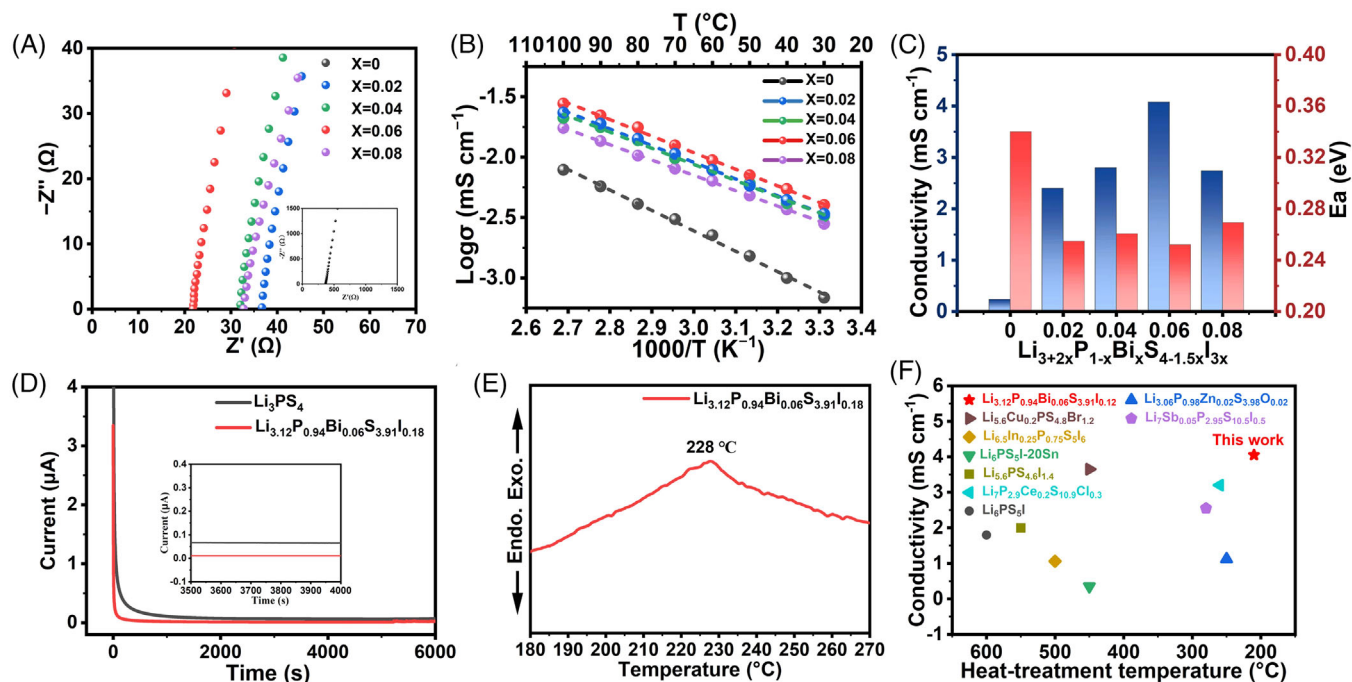
**FIGURE 2** Li^+ ion dynamics of $Li_{3.12}P_{0.94}Bi_{0.06}S_{3.91}I_{0.18}$ SSEs. (A) The impendence plots of $Li_{3+2x}P_{1-x}Bi_xS_{4-1.5x}I_{3x}$ ($x = 0.02$, 0.04, 0.06, and 0.08) SSEs at room temperature. (B) Arrhenius plots and (C) the relation between the ionic conductivity and activation energy of $Li_{3+2x}P_{1-x}Bi_xS_{4-1.5x}I_{3x}$ ($x = 0$, 0.02, 0.04, 0.06, and 0.08). (D) Direct current (DC) polarization current-time curves of $Li_{3+2x}P_{1-x}Bi_xS_{4-1.5x}I_{3x}$ ($x = 0$ and 0.06) SSEs at a constant voltage of 1 V. (E) Differential thermal analysis (DTA) curve of $Li_{3.12}P_{0.94}Bi_{0.06}S_{3.91}I_{0.18}$ in an argon atmosphere from 180°C to 270°C. (F) Thermal treatment temperature and corresponding ionic conductivity comparison of our $Li_{3.12}P_{0.94}Bi_{0.06}S_{3.91}I_{0.18}$ with several reported sulfide SSEs.

225 h owing to its poor Li compatibility (Figure S9a,b). Additionally, the Li|$Li_{3.12}P_{0.94}Bi_{0.06}S_{3.91}I_{0.18}$|Li symmetric cell can cycle steadily at a high current density of 0.25 mA cm^{-2} (Figure S10). This indicates that the doping of Bi^{3+} can inhibit the reaction between electrolyte and lithium dendrites. Moreover, the linear sweep voltammetry profiles from open-circuit voltage to 0 V of Li|SSEs|SSEs/C cells at 0.1 mV s^{-1} were conducted to evaluate the electrochemical stability of the SSEs with lithium metal anode. Both SSEs started to decrease near the open-circuit voltage, and a significant increase in the specific current with a high integral reduction current (0.11768 VA g^{-1}) was observed for the Li_3PS_4. However, the reduction potential of $Li_{3.12}P_{0.94}Bi_{0.06}S_{3.91}I_{0.18}$ slightly increased (2.197 V) with an integral current of only 0.08508 A g^{-1}, indicating the superior Li compatibility of $Li_{3.12}P_{0.94}Bi_{0.06}S_{3.91}I_{0.18}$ (Figure S11). The chemical stability of Li metal and $Li_{3.12}P_{0.94}Bi_{0.06}S_{3.91}I_{0.18}$ SSEs was further examined by XPS measurement. As shown in Figure 3E,F, distinct Li_2S (159.8 eV), reduced P (130.8 eV), and Li_3P (127 and 128.5 eV) peaks appear after 100 cycles at the Li|Li_3PS_4 interface, indicating a severe reduction of Li_3PS_4 by Li metal (Figure S12). However, a negligible amount of Li_2S and Li_3P with a low-intensity signal is detected on the Li|$Li_{3.12}P_{0.94}Bi_{0.06}S_{3.91}I_{0.18}$ interface, along with a stable

Li–Bi alloy formation (Figure S12a), suggesting that the co-doping of Bi and I significantly enhances interfacial compatibility with Li metal.[14] Additionally, the increased amount of LiI (630.2 and 618.8 eV) after cycling effectively passivates the active Li metal and inhibits the growth of Li dendrites (Figures 3G, S12b, and S4).[37]

To validate the air stability of $Li_{3+2x}P_{1-x}Bi_xS_{4-1.5x}I_{3x}$, this SSE was placed in a sealed container at a temperature of 25°C and a humidity of 35%. The stability of SSE in the air was determined by monitoring the amount of H_2S released from SSEs at different time by an online H_2S detector (Figure 4A). It is found that $Li_{3.12}P_{0.94}Bi_{0.06}S_{3.91}I_{0.18}$ shows minimal change with the H_2S concentration of only 0.205 cm^3 g^{-1} after 300 min, after which H_2S concentration remains constant thenceforth. In contrast, Li_3PS_4 exhibits a higher concentration of 0.632 cm^3 g^{-1} at the same time, and the steep slope of the curve indicates a faster H_2S release rate. Additionally, it is disclosed that $Li_{3.12}P_{0.94}Bi_{0.06}S_{3.91}I_{0.18}$ maintains its lamellar shape even after 300 min of exposure to humid air, whereas Li_3PS_4 experiences severe structural collapse under the same condition, demonstrating the uniqueness of Bi and I co-doping in improving air stability of this sulfide SSE (Figure S13). In addition, structural changes in the SSEs were examined via XRD tests after 20 min
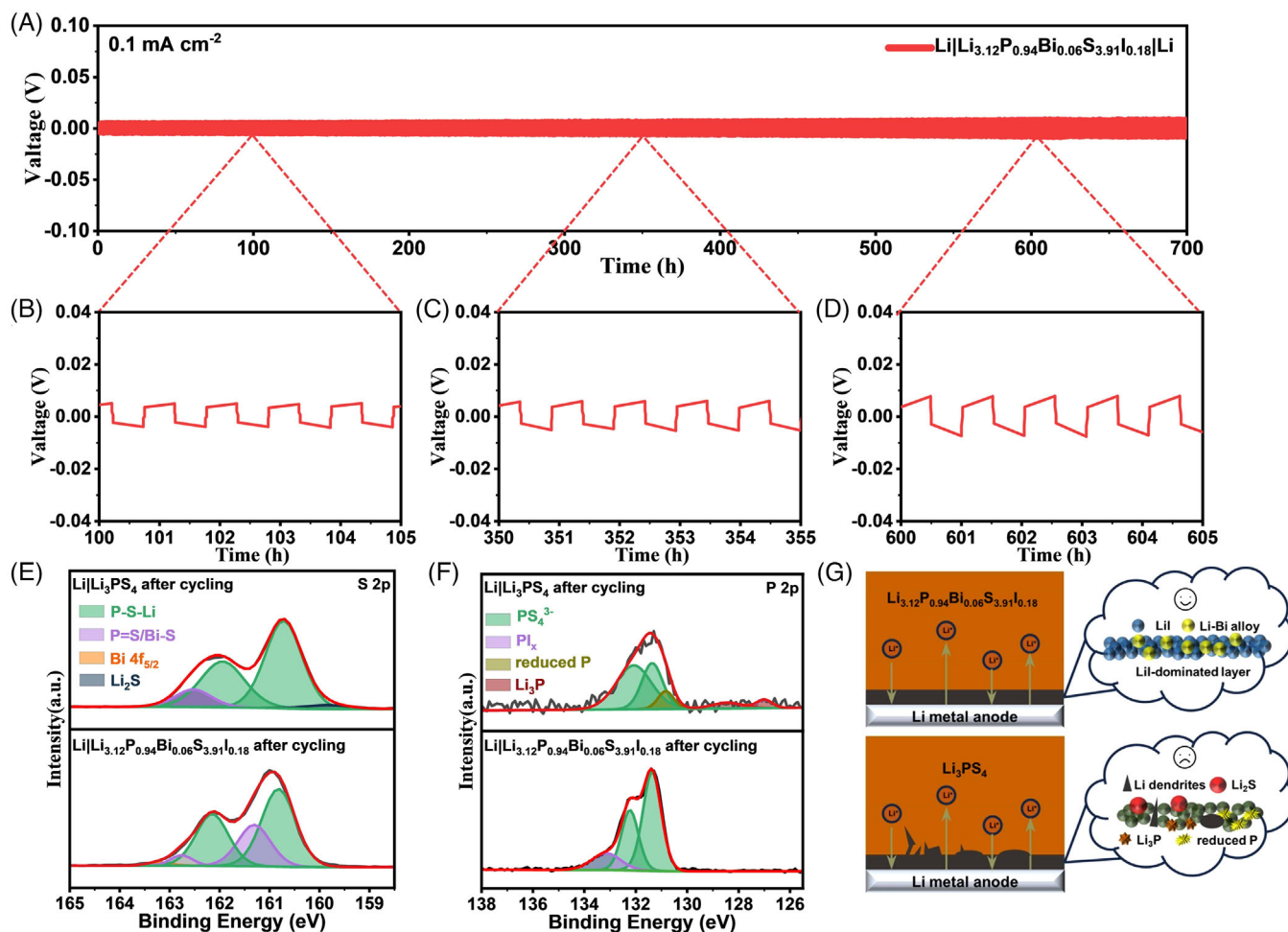
FIGURE 3 Performance and characterization of Li|Li$_{3.12}$P$_{0.94}$Bi$_{0.06}$S$_{3.91}$I$_{0.18}$|Li symmetric cells. (A) Galvanostatic cycling of Li plating/stripping profile for Li|Li$_{3.12}$P$_{0.94}$Bi$_{0.06}$S$_{3.91}$I$_{0.18}$|Li symmetric cell at 0.1 mA cm^{-2} and 0.1 mAh cm^{-2}. (BandD) Magnified Li plating/stripping profiles for the cycling periods of (B) 100–105 h, (C) 350–355 h, and (D) 600–605 h. (E and F) X-ray photoelectron spectroscopy (XPS) spectra of (E) S 2p and (F) P 2p for Li$_3$PS$_4$ and Li$_{3.12}$P$_{0.94}$Bi$_{0.06}$S$_{3.91}$I$_{0.18}$ SSEs after the Li plating/stripping for 100 cycles. (G) The solid electrolyte interface (SEI) formation mechanism diagram induced by Li$_{3.12}$P$_{0.94}$Bi$_{0.06}$S$_{3.91}$I$_{0.18}$ and Li$_3$PS$_4$ SSEs on Li metal anodes.

of exposure to moist air. Impressively, the XRD peaks of Li$_{3.12}$P$_{0.94}$Bi$_{0.06}$S$_{3.91}$I$_{0.18}$ remain almost unchanged compared to the pristine sample, indicating that the doping of Bi significantly improves the hydrolysis resistance of Li$_3$PS$_4$-based SSEs. However, a change in the peak shape and the appearance of several new impurity peaks can be observed in the XRD pattern of Li$_3$PS$_4$ (Figure 4B), suggesting partial structural and compositional change of PS$_4^{3-}$ induced by hydrolysis. Notably, the exceptionally high air stability of Li$_{3.12}$P$_{0.94}$Bi$_{0.06}$S$_{3.91}$I$_{0.18}$ (0.205 cm^3 g^{-1}) is superior to that of the most reported representative air-stable sulfide SSEs (Table S3), such as Li$_{6.988}$P$_{2.994}$Nb$_{0.2}$S$_{10.934}$O$_{0.6}$ (0.489 cm^3 g^{-1}),[29] Li$_7$P$_{2.9}$Sb$_{0.1}$S$_{10.75}$O$_{0.25}$ (1.02 cm^3 g^{-1}),[38] Li$_7$P$_{2.9}$Ce$_{0.2}$S$_{10.9}$Cl$_{0.3}$ (3.12 cm^3 g^{-1}),[39] Li$_4$SnS$_4$ (0.25 cm^3 g^{-1}),[40] and Li$_{6.3}$P$_{0.9}$Cu$_{0.1}$S$_{4.9}$Cl$_{1.1}$ (0.49 cm^3 g^{-1}).[41] Therefore, the partial replacement of the hard acid P with soft acid Bi can greatly enhance the hydrolysis resistance of

Li$_3$PS$_4$-based SSEs, demonstrating its high potential for practical application (Figure 4C).

To insightfully understand the improved air stability of Bi-doped Li$_3$PS$_4$, the density generalized function theory calculation was employed to assess both the water hydrolysis reaction energy (ΔE_{hy}) and adsorption energy (ΔE_{ad}) (Figure 4D). The hydrolysis reaction of sulfide SSEs typically involves PS$_4$ structural units reaction with H$_2$O. In the case of the Li$_{3.12}$P$_{0.94}$Bi$_{0.06}$S$_{3.91}$I$_{0.18}$, two sulfur-containing structural units (PS$_4$ and BiS$_4$), along with the sulfur-containing structural unit PS$_3$O generated after the hydrolysis reaction, are formed when considering the substitution of Bi at the P-position. Notably, the PS$_4$ has a relatively low ΔE_{hy} (-2.56 eV) and ΔE_{ad} (-0.33 eV), implying its facile reaction with H$_2$O (Tables S1 and S2). On the contrary, the positive value of ΔE_{hy} (1.16 eV) indicates that the hydrolysis reaction of Li$_{3.12}$P$_{0.94}$Bi$_{0.06}$S$_{3.91}$I$_{0.18}$ SSEs is
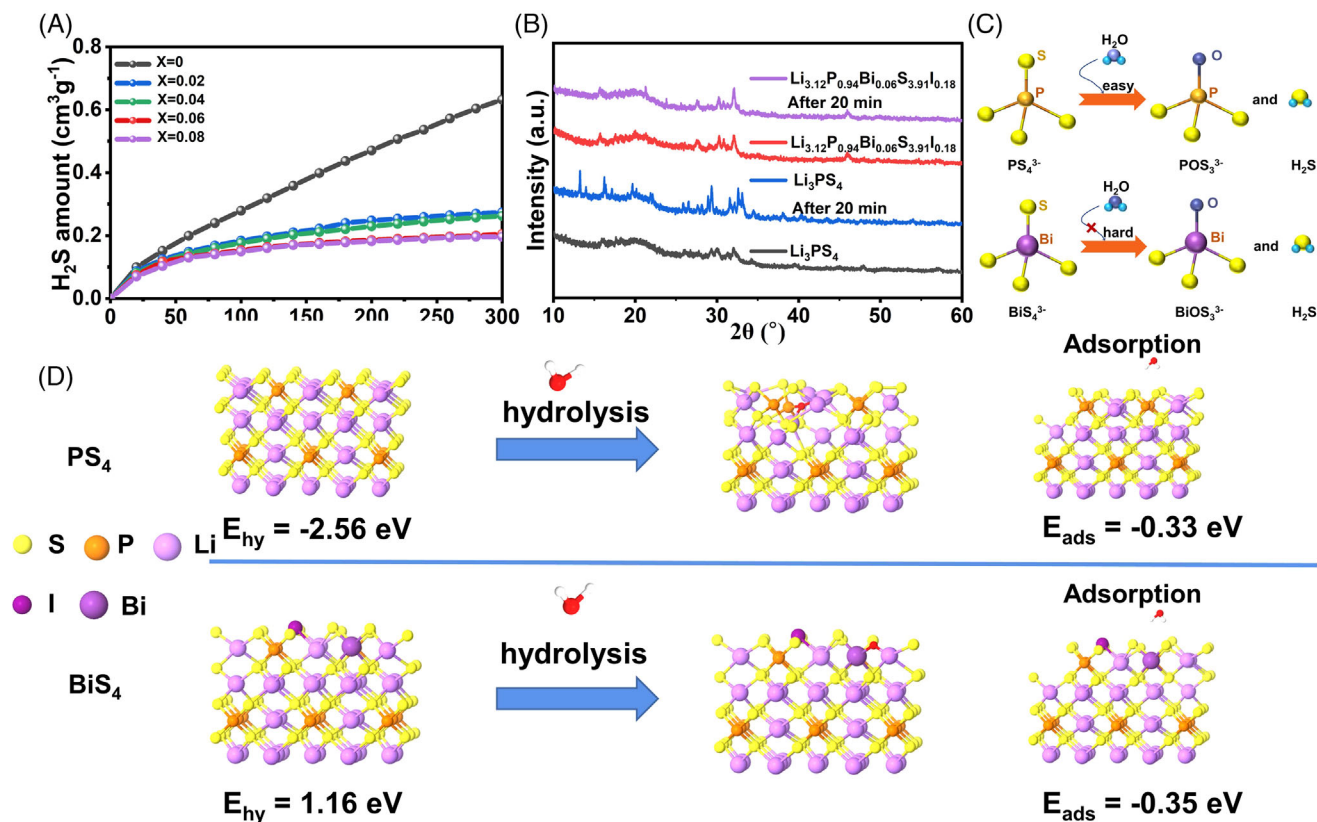
FIGURE 4 The air stability of $Li_{3.12}P_{0.94}Bi_{0.06}S_{3.91}I_{0.18}$ solid-state electrolytes (SSEs). (A) The amounts of H_2S generated from $Li_{3+2x}P_{1-x}Bi_xS_{4-1.5x}I_{3x}$ ($x = 0, 0.02, 0.04, 0.06,$ and 0.08) when exposed to wet air. (B) X-ray diffraction (XRD) patterns of Li_3PS_4 and $Li_{3.12}P_{0.94}Bi_{0.06}S_{3.91}I_{0.18}$ after exposure to wet air for 20 min. (C) Schematic diagram of Li_3PS_4 and $Li_{3.12}P_{0.94}Bi_{0.06}S_{3.91}I_{0.18}$ when reacted with H_2O. (D) The calculated model of adsorption and reaction energies of one water molecule on PS_4 and BiS_4 units.

thermodynamically unfavorable (Figure 4C), which is consistent with previous experimental results on the enhanced air stability of $Li_{3.12}P_{0.94}Bi_{0.06}S_{3.91}I_{0.18}$.

To evaluate the applicability of SSEs, the as-synthesized $Li_{3.12}P_{0.94}Bi_{0.06}S_{3.91}I_{0.18}$ and Li_3PS_4 SSEs were assembled into ASSLMBs using Nb_2O_5-coated $LiNi_{0.8}Mn_{0.1}Co_{0.1}O_2$ ($NCM811@Nb_2O_5$) cathode and Li metal anode. $Li_{10}GeP_2S_{12}$ SSEs (LGPS) are used as catholytes to ensure sufficient ionic conductivity (Figures 5A and S14). The cells were initially cycled at a constant current of 0.1 C (1 C = 200 mAh g^{-1}) in the voltage range of 3.0–4.3 V at 60°C. Figure S15 exhibits the typical charge-discharge voltage curves of the ASSLMBs. The initial discharge capacity of ASSLMBs with $Li_{3.12}P_{0.94}Bi_{0.06}S_{3.91}I_{0.18}$ SSE is 163.6 mAh g^{-1} with a high coulombic efficiency of 79.5%. Importantly, a high capacity retention rate of 86.8% is maintained after 80 cycles. By contrast, as for the battery with the Li_3PS_4, the capacity is only 77 mAh g^{-1} with a low capacity retention of 60.3% after 15 cycles (Figures 5B and S16). Moreover, a significant voltage polarization with a low initial coulombic efficiency of only 55.35% is observed. Furthermore, the discharge capacities of the $NCM811@Nb_2O_5|LGPS|Li_{3.12}P_{0.94}Bi_{0.06}S_{3.91}I_{0.18}|Li$ cell are

169, 136, 115, 105, and 87 mAh g^{-1} at 0.05, 0.1, 0.2, 0.3, and 0.5 C (Figure 5C,D), respectively, and the capacity can recover to 140 mAh g^{-1} when the current density shifts back to 0.1 C, suggesting excellent rate capability of the $Li_{3.12}P_{0.94}Bi_{0.06}S_{3.91}I_{0.18}$ electrolyte-based ASSLMBs. Besides, the cyclability of ASSLMBs was also measured at room temperature. As depicted in Figures 5E and S17, the $NCM811@Nb_2O_5|LGPS|Li_{3.12}P_{0.94}Bi_{0.06}S_{3.91}I_{0.18}|Li$ cell shows a reversible capacity of 111 mAh g^{-1} and impressive capacity retention of 95.8% after 300 cycles at 0.1 C, which is superior to those of most reported sulfide-based ASSLMBs, such as $NCM622|Li_6PS_5Cl–Li_2ZrCl_6|Li$ (0.3 C, 70 cycles, capacity retention 87.10%),[42] $NCM532@LNO|Li_6P_{0.925}Sb_{0.075}S_5Cl|Li$ (0.2 C, 60 cycles, capacity retention 82.60%),[43] and $NCM523@LNO|Li_{6.04}P_{0.98}Bi_{0.02}S_{4.97}O_{0.03}Cl|Li$ (0.1 C, 60 cycles, capacity retention 88.60%) (Tables S4).[44]

Subsequently, an in situ impedance test was conducted on the ASSLMBs to elucidate the underlying electrochemical distinctions. The charge and discharge processes were examined at various cut-off voltages. During the charging process, the increase in the cut-off voltages results in a higher total impedance for both
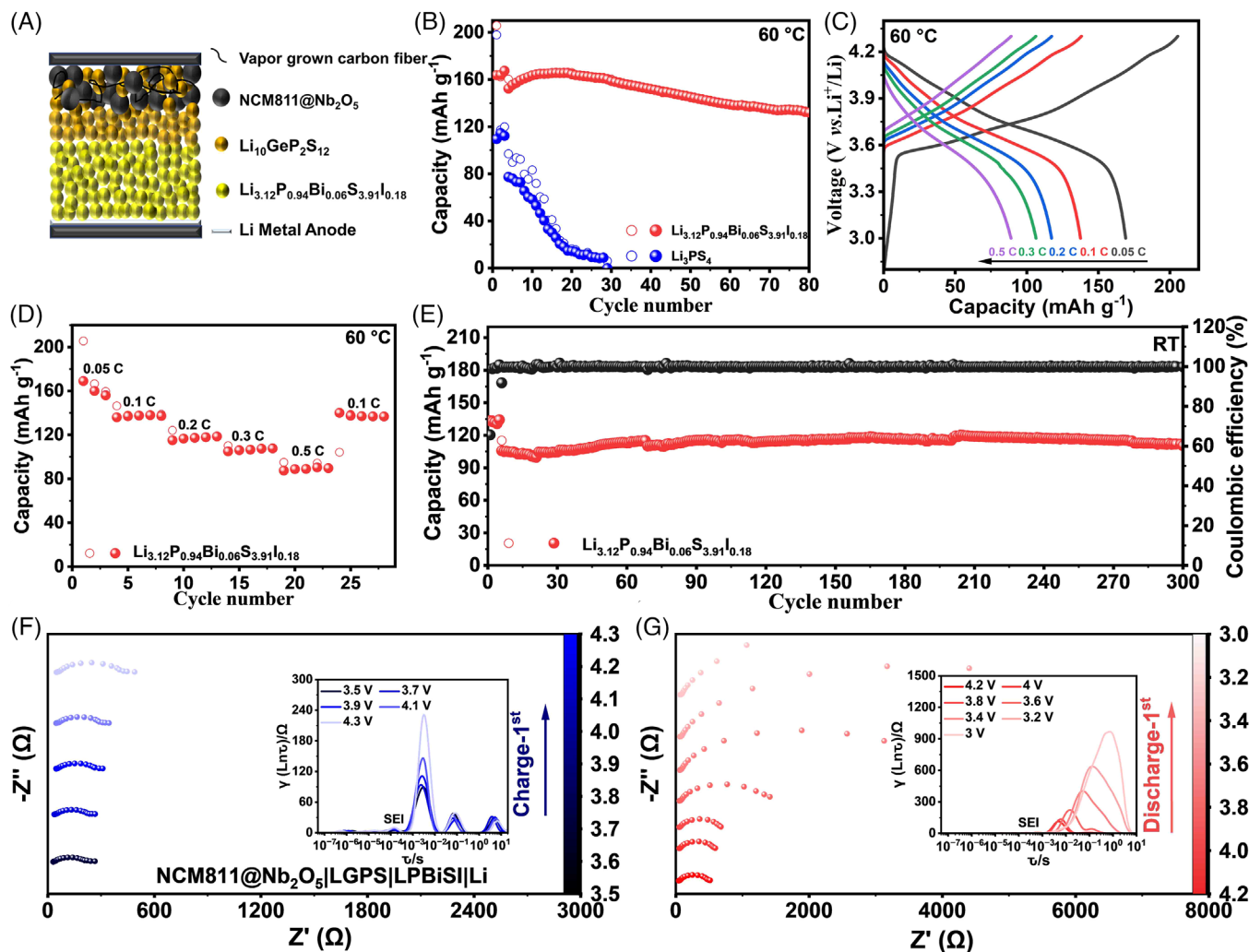
FIGURE 5 Electrochemical performance of $Li_{3.12}P_{0.94}Bi_{0.06}S_{3.91}I_{0.18}$-based all-solid-state lithium metal batteries (ASSLMBs). (A) Schematic diagram of NCM811@Nb_2O_5|LGPS|$Li_{3.12}P_{0.94}Bi_{0.06}S_{3.91}I_{0.18}$|Li ASSLMBs. (B) Cyclic performance of NCM811@Nb_2O_5|LGPS|Li_3PS_4|Li and NCM811@Nb_2O_5|LGPS|$Li_{3.12}P_{0.94}Bi_{0.06}S_{3.91}I_{0.18}$|Li cells obtained at 0.1 C (1 C = 200 mAh g^{-1}) at 60°C between 3.0 and 4.3 V. (C) Galvanostatic charge and discharge profiles and (D) rate capability of NCM811@Nb_2O_5|LGPS|$Li_{3.12}P_{0.94}Bi_{0.06}S_{3.91}I_{0.18}$|Li cell from 0.1 to 0.5 C measured at 60°C. (E) The cycling performance of NCM811@Nb_2O_5|LGPS|$Li_{3.12}P_{0.94}Bi_{0.06}S_{3.91}I_{0.18}$|Li cell at 0.1 C and 25°C. (F and G) Interfacial impedance evolution and the corresponding distribution of relaxation time (DRT) profiles under different (F) states of charge (SOC) and (G) states of discharge (SOD) in the first cycle.

batteries (Figures 5F and S18a). In the discharge process, the total impedances of both battery setups significantly increase at shallower discharge depths (Figures 5G and S18b), aligning with findings from previous studies.[45] It is evident that NCM811@Nb_2O_5|LGPS|Li_3PS_4|Li maintains a high initial impedance, and the impedance of the battery is significantly increased during the subsequent charge and discharge process. In contrast, NCM811@Nb_2O_5LGPS|$Li_{3.12}P_{0.94}Bi_{0.06}S_{3.91}I_{0.18}$|Li exhibited a lower initial impedance (265 Ω), attributed to the higher ionic conductivity of $Li_{3.12}P_{0.94}Bi_{0.06}S_{3.91}I_{0.18}$. Additionally, as the depth of subsequent charge and discharge processes increases, the $Li_{3.12}P_{0.94}Bi_{0.06}S_{3.91}I_{0.18}$-based battery sustains lower impedance due to the formation of

a stable SEI between SSE and Li metal without serious side reactions. To gain more intuitive understanding of resistance changes of the battery during different states of charge (SOC) and states of discharge (SOD) preprocess, the distribution of relaxation time curves was analyzed.[44] In terms of time constant, the bulk resistance ($R_{SE-bulk}$) of the solid electrolyte layer is distributed between 10^{-7} and 10^{-6} s, and Li_3PS_4 shows higher bulk resistance than that of $Li_{3.12}P_{0.94}Bi_{0.06}S_{3.91}I_{0.18}$, corresponding to its larger initial impedance. The grain boundary impedance between the solid electrolyte particles is roughly distributed between 10^{-6} and 10^{-5} s, and these two batteries maintain low impedance. The impedance of SEI falls in the range of 10^{-4} to 10^{-3} s (Figures 5F and S18a).

Compared to the $NCM811@Nb_2O_5|LGPS|Li_3PS_4|Li$, which has a high impedance, the SEI impedance of $NCM811@Nb_2O_5|LGPS|Li_{3.12}P_{0.94}Bi_{0.06}S_{3.91}I_{0.18}|Li$ remains extremely low (5.3–10.1 Ω) during the charge and discharge processes (Figure 5F,G). This is mainly attributed to the formation of a stable SEI layer, further demonstrating excellent interfacial compatibility of $Li|Li_{3.12}P_{0.94}Bi_{0.06}S_{3.91}I_{0.18}$ during long-term cycling.[46]

3 | CONCLUSION

In summary, we report an air-stable $Li_{3.12}P_{0.94}Bi_{0.06}S_{3.91}I_{0.18}$ glass-ceramic SSE obtained by co-doping Li_3PS_4 with Bi and I for high-performance ASSLMBs. Owing to the increased Li^+ concentration, weakened electronegativity between Li^+ and S^{2-}, and anion site-disorder induced from I, the resulting SSE shows greatly enhanced ionic conductivity of 4.05 mS cm^{-1}. Furthermore, the introduction of BiI also improved the Li dendrite suppression capability and air stability induced from the in situ formed robust SEI (LiI and Li–Bi alloy) and strong covalent bonding of Bi–S bonds. Consequently, the Li symmetric cell-based $Li_{3.12}P_{0.94}Bi_{0.06}S_{3.91}I_{0.18}$ SSEs shows an ultrahigh CCD value of 0.9 mA cm^{-2} and ultralong cyclability of 700 h at 0.1 mA cm^{-2}. The corresponding ASSLMBs exhibit a high discharge capacity of 111 mAh g^{-1}, and remain 95.8% of the initial capacity after 300 cycles at 0.1 C. This work demonstrates that the Bi and I co-doping strategy is a reliable direction to develop air-stable sulfide-based SSEs for ASSLMBs with high energy density and long cyclability.

4 | EXPERIMENTAL

The experimental details and characterizations are provided in the Supporting Information.

CONFLICT OF INTEREST STATEMENT
The authors declare no conflict of interest.

ORCID
Yanfeng Dong https://orcid.org/0000-0002-4916-428X
Zhong-Shuai Wu https://orcid.org/0000-0003-1851-4803

REFERENCES

1. Chen R, Li Q, Yu X, Chen L, Li H. Approaching practically accessible solid-state batteries: stability issues related to solid electrolytes and interfaces. *Chem Rev*. 2020;120(14):6820-6877.
2. Xia W, Zhao Y, Zhao F, et al. Antiperovskite electrolytes for solid-state batteries. *Chem Rev*. 2022;122(3):3763-3819.
3. Zhao Q, Liu X, Stalin S, Khan K, Archer LA. Solid-state polymer electrolytes with in-built fast interfacial transport for secondary lithium batteries. *Nat Energy*. 2019;4(5):365-373.
4. Zhao B-S, Chen P, Gao X-P. Bulk and interface-strengthened $Li_7P_{2.9}Sb_{0.1}S_{10.65}O_{0.15}I_{0.2}$ electrolyte via dual-source doping for all-solid-state lithium-sulfur batteries. *Sci China Mater*. 2022;66(2):513-521.
5. Lee YG, Fujiki S, Jung C, et al. High-energy long-cycling all-solid-state lithium metal batteries enabled by silver–carbon composite anodes. *Nat Energy*. 2020;5(4):299-308.
6. Xu R, Han F, Ji X, Fan X, Tu J, Wang C. Interface engineering of sulfide electrolytes for all-solid-state lithium batteries. *Nano Energy*. 2018;53:958-966.
7. Su Y, Zhang X, Du C, et al. An all-solid-state battery based on sulfide and PEO composite electrolyte. *Small*. 2022;18(29):2202069.
8. Gil-González E, Ye L, Wang Y, et al. Synergistic effects of chlorine substitution in sulfide electrolyte solid state batteries. *Energy Storage Mater*. 2022;45:484-493.
9. Zhou X, Zhang Y, Shen M, et al. A highly stable Li-organic all-solid-state battery based on sulfide electrolytes. *Adv Energy Mater*. 2022;12(14):2103932.
10. Yang Z, Wang F, Hu Z, et al. Room-temperature all-solid-state lithium–organic batteries based on sulfide electrolytes and organodisulfide cathodes. *Adv Energy Mater*. 2021;11(48):2102962.
11. Li X, Liang J, Li X, et al. High-performance all-solid-state Li–Se batteries induced by sulfide electrolytes. *Energy Environ Sci*. 2018;11(10):2828-2832.
12. Otoyama M, Sakuda A, Tatsumisago M, Hayashi A. Sulfide electrolyte suppressing side reactions in composite positive electrodes for all-solid-state lithium batteries. *ACS Appl Mater Interfaces*. 2020;12(26):29228-29234.

13. Zeng D, Yao J, Zhang L, et al. Promoting favorable interfacial properties in lithium-based batteries using chlorine-rich sulfide inorganic solid-state electrolytes. *Nat Commun*. 2022;13(1):1909.

14. Kato Y, Hori S, Saito T, et al. High-power all-solid-state batteries using sulfide superionic conductors. *Nat Energy*. 2016;1(4):16030.

15. Ni Y, Huang C, Liu H, Liang Y, Fan LZ. A high air-stability and Li-metal-compatible $Li_{3+2x}P_{1-x}Bi_xS_{4-1.5x}O_{1.5x}$ sulfide electrolyte for all-solid-state Li–metal batteries. *Adv Funct Mater*. 2022;32(41):2205998.

16. Lee JE, Park KH, Kim JC, et al. Universal solution synthesis of sulfide solid electrolytes using alkahest for all-solid-state batteries. *Adv Mater*. 2022;34(16):2200083.

17. Zuo TT, Walther F, Ahmed S, et al. Formation of an artificial cathode–electrolyte interphase to suppress interfacial degradation of Ni-rich cathode active material with sulfide electrolytes for solid-state batteries. *ACS Energy Lett*. 2023;8(3):1322-1329.

18. Jung SK, Gwon H, Lee SS, et al. Understanding the effects of chemical reactions at the cathode–electrolyte interface in sulfide based all-solid-state batteries. *J Mater Chem A*. 2019;7(40):22967-22976.

19. Oh P, Yun J, Choi JH, et al. Development of high-energy anodes for all-solid-state lithium batteries based on sulfide electrolytes. *Angew Chem Int Ed*. 2022;61(25):202201249.

20. Yan W, Mu Z, Wang Z, et al. Hard-carbon-stabilized Li–Si anodes for high-performance all-solid-state Li-ion batteries. *Nat Energy*. 2023;8(8):800-813.

21. Ma Y, Wang L, Fu S, et al. Situ formation of a Li–Sn alloy protected layer for inducing lateral growth of dendrites. *J Mater Chem A*. 2020;8(44):23574-23579.

22. Kang J, Deng N, Liu Y, et al. Recent advances of anode protection in solid-state lithium metal batteries. *Energy Storage Mater*. 2022;52:130-160.

23. Li Y, Arnold W, Thapa A, et al. Stable and flexible sulfide composite electrolyte for high-performance solid-state lithium batteries. *ACS Appl Mater Interfaces*. 2020;12(38):42653-42659.

24. Lu P, Wu D, Chen L, Li H, Wu F. Air stability of solid-state sulfide batteries and electrolytes. *Electrochem Energy Rev*. 2022;5(3).

25. Liu H, Liang Y, Wang C, et al. Priority and prospect of sulfide-based solid-electrolyte membrane. *Adv Mater*. 2023;35(50):2206013.

26. Rajagopal R, Cho JU, Subramanian Y, et al. Preparation of highly conductive metal doped/substituted $Li_7P_2S_8Br_{1-x}I_x$ type lithium superionic conductor for all-solid-state lithium battery applications. *Chem Eng J*. 2022;428:13215.

27. Liu G, Xie D, Wang X, et al. High air-stability and superior lithium ion conduction of $Li_{3+3x}P_{1-x}Zn_xS_{4-x}O_x$ by aliovalent substitution of ZnO for all-solid-state lithium batteries. *Energy Storage Mater*. 2019;17:266-274.

28. Jiang Z, Liu Y, Peng H, et al. Enhanced air stability and interfacial compatibility of Li-argyrodite sulfide electrolyte triggered by CuBr co-substitution for all-solid-state lithium batteries. *Energy Storage Mater*. 2023;56:300-309.

29. Ahmad N, Zhou L, Faheem M, et al. Enhanced air stability and high Li-ion conductivity of $Li_{6.988}P_{2.994}Nb_{0.2}S_{10.934}O_{0.6}$ glass-ceramic electrolyte for all-solid-state lithium–sulfur batteries. *ACS Appl Mater Interfaces*. 2020;12(19):21548-21558.

30. Lu P, Liu L, Wang S, et al. Superior all-solid-state batteries enabled by a gas-phase-synthesized sulfide electrolyte with ultrahigh moisture stability and ionic conductivity. *Adv Mater*. 2021;33(32):2100921.

31. Rui X, Ren D, Liu X, et al. Distinct thermal runaway mechanisms of sulfide-based all-solid-state batteries. *Energy Environ Sci*. 2023;16(8):3552-3563.

32. Ma T, Wang Z, Wu D, et al. High-areal-capacity and long-cycle-life all-solid-state battery enabled by freeze drying technology. *Energy Environ Sci*. 2023;16(5):2142-2152.

33. Crapse J, Pappireddi N, Gupta M, Shvartsman SY, Wieschaus E, Wuhr M. Evaluating the Arrhenius equation for developmental processes. *Mol Syst Biol*. 2021;17(8):9895.

34. Lu P, Xia Y, Huang Y, et al. Wide-temperature, long-cycling, and high-loading pyrite all-solid-state batteries enabled by argyrodite thioarsenate superionic conductor. *Adv Funct Mater*. 2022;33(8):2211211.

35. Hong M, Dong Q, Xie H, et al. Ultrafast sintering of solid-state electrolytes with volatile fillers. *ACS Energy Lett*. 2021;6(11):3753-3760.

36. Kim MJ, Choi IH, Jo SC, et al. A novel strategy to overcome the hurdle for commercial all-solid-state batteries via low-cost synthesis of sulfide solid electrolytes. *Small Methods*. 2021;5(11):2100793.

37. Yi S, Su Z, Zhang W, et al. An ion-released MgI_2-doped separator inducing a LiI-containing solid electrolyte interphase for dendrite-free Li metal anodes. *J Energy Chem*. 2022;75:83-94.

38. Zhao BS, Wang L, Chen P, et al. Congener substitution reinforced $Li_7P_{2.9}Sb_{0.1}S_{10.75}O_{0.25}$ glass-ceramic electrolytes for all-solid-state lithium-sulfur batteries. *ACS Appl Mater Interfaces*. 2021;13(29):34477-34485.

39. Zhou L, Tufail MK, Ahmad N, Song T, Chen R, Yang W. Strong interfacial adhesion between the Li_2S cathode and a functional $Li_7P_{2.9}Ce_{0.2}S_{10.9}Cl_{0.3}$ solid-state electrolyte endowed long-term cycle stability to all-solid-state lithium–sulfur batteries. *ACS Appl Mater Interfaces*. 2021;13(24):28270-28280.

40. Kanazawa K, Yubuchi S, Hotehama C, et al. Mechanochemical synthesis and characterization of metastable hexagonal $Li_{(4)}SnS_{(4)}$ solid electrolyte. *Inorg Chem*. 2018;57(16):9925-9930.

41. Taklu BW, Su WN, Nikodimos Y, et al. Dual CuCl doped argyrodite superconductor to boost the interfacial compatibility and air stability for all solid-state lithium metal batteries. *Nano Energy*. 2021;90:106542.

42. Zhang H, Yu Z, Cheng J, Chen H, Huang X, Tian B. Halide/sulfide composite solid-state electrolyte for Li-anode based all-solid-state batteries. *Chin Chem Lett*. 2023;34(11):108228.

43. Liu H, Zhu Q, Liang Y, et al. Versatility of Sb-doping enabling argyrodite electrolyte with superior moisture stability and Li metal compatibility towards practical all-solid-state Li metal batteries. *Chem Eng J*. 2023;462:142183.

44. Liu H, Zhu Q, Wang C, et al. High air stability and excellent Li metal compatibility of argyrodite-based electrolyte enabling superior all-solid-state Li metal batteries. *Adv Funct Mater*. 2022;32(32):2203858.

45. Wei C, Liu X, Yu C, et al. Revealing performance of $78Li_2S–22P_2S_5$ glass ceramic based solid-state batteries at different operating temperatures. *Chin Chem Lett*. 2023;34(7):107859.

46. Lu Y, Zhao CZ, Huang JQ, Zhang Q. The timescale identification decoupling complicated kinetic processes in lithium batteries. *Joule*. 2022;6(6):1172-1198.

SUPPORTING INFORMATION

Additional supporting information can be found online in the Supporting Information section at the end of this article.